Correspondence

Autonomous Ground Vehicle Path Planning in Urban Environments Using GNSS and Cellular Signals Reliability Maps: Simulation and Experimental Results

A framework for autonomous ground vehicle (AGV) path planning using global navigation satellite systems (GNSS) signals and cellular long-term evolution (LTE) signals is evaluated through several simulations and experiments. The objective of path planning is to prescribe the optimal path for the AGV to follow to reach a desired target point. Optimality is defined as the shortest distance, while minimizing the AGV's position estimation error and guaranteeing that the uncertainty about its position is below a desired threshold. Path planning is prescribed via signal reliability maps, which provide information about regions where large errors due to cellular signal multipath or obstructed GNSS line-of-sight are expected. Simulation results are presented demonstrating that utilizing ambient cellular LTE signals together with GNSS signals 1) reduces the uncertainty about the AGV's position, 2) increases the number of feasible paths to choose from, which could be useful if other considerations arise (e.g., traffic jams and road blockages due to construction), and 3) yields significantly shorter feasible paths, which would otherwise be infeasible with GNSS signals alone. Experimental results on a ground vehicle navigating in downtown Riverside, CA, USA, are presented demonstrating a close match between the simulated and experimental results.

I. INTRODUCTION

To ensure safe and efficient operation of future autonomous ground vehicles (AGVs), one must establish performance guarantees prior to their deployment into the environment. These performance guarantees consider the AGV's sensing and computation capabilities as well as environmental factors (e.g., road map, traffic, weather, time of day, etc.). Issues pertaining to perception, navigation, and control of AGVs become increasingly coupled [1], [2]. In this respect, an AGV could plan its path, which may temporarily detract it from its desired final destination, in exchange for improving its situational awareness and guaranteeing desired safety measures [3].

Manuscript received October 22, 2020; revised January 6, 2021; released for publication January 17, 2021. Date of publication January 26, 2021; date of current version August 9, 2021.

DOI. No. 10.1109/TAES.2021.3054684

Refereeing of this contribution was handled by O. Osechas.

This work was supported in part by the Office of Naval Research (ONR) under Grant N00014-19-1-2613 and in part by the National Science Foundation (NSF) under Grant 1929571 and Grant 1929965.

Authors. addresses: Sonya Ragothaman was with the Department of Electrical and Computer Engineering, University of California, Riverside, CA 92507 USA, and is now with the Aerospace Corporation, University of California, El Segundo, CA 90245 USA, E-mail: (sonya.ragothaman@gmail.com); Mahdi Maaref and Zaher M. Kassas are with the Department of Mechanical and Aerospace Engineering, University of California, Irvine, CA 92521 USA, E-mail: (mmaaref@uci.edu; zkassas@ieee.org). *(Corresponding author: Zaher M. Kassas.)*

This article considers the following problem, originally defined in [4] and [5]. An AGV is equipped with receivers capable of producing pseudoranges to overhead global navigation satellite system (GNSS) satellites (e.g., [6]–[9]) and to cellular long-term evolution (LTE) base stations in its environment (e.g., [10]–[13]). The AGV fuses these pseudoranges to estimate its position and clock bias. The AGV is also equipped with a 3-D building map of the environment (e.g., [14], [15]). Starting from a known point, the AGV desires to reach a target point by taking the shortest path, while minimizing the AGV's position estimation error and guaranteeing that the uncertainty about its position is below a desired threshold. Toward this objective, a signal reliability map is first generated that specifies which signals are reliable to use at different locations and at different times in the environment. Each point in the environment has a corresponding signal reliability (a boolean measure) for the different overhead GNSS satellites and nearby cellular base stations. A reliable GNSS satellite means that there exists an unobstructed line-of-sight (LOS) to that satellite. A reliable cellular base station means that the pseudorange bias due to multipath is below a certain threshold. Next, equipped with this signal reliability map, a path planning generator produces 1) the optimal path to the target point, if any, and 2) other feasible paths the AGV could take. These suboptimal, yet feasible, paths could be useful should the AGV choose to not follow the optimal path, e.g., to avoid traffic jams and road blockages due to construction or emergency. A table specifying the reliable GNSS satellites and cellular base stations to use along the optimal and feasible paths is also generated. Two path planning algorithms are considered: One which is suitable for short travel times and assumes that the GNSS satellite geometry is fixed, while the other is suitable for long travel times and considers GNSS satellite motion. The second algorithm is more computationally involved. The prequel of this article surveyed related work and presented relevant models, analytical derivations, and algorithm development [5]. This article presents comprehensive simulation and experimental studies for different realistic scenarios to evaluate the accuracy and efficacy of the proposed approach on an AGV navigating in a deep urban environment.

This article is organized as follows. Section II gives an overview of the different driving scenarios considered in this article. Sections III and IV present simulation and experimental results evaluating the performance of the path planning approach, respectively. Finally, Section V concludes this article.

II. SCENARIOS OVERVIEW

The simulation study considers three different AGV driving scenarios, in which we have the following.

1) Scenarios 1 and 2 compare the feasible paths for two AGVs, where one of the AGVs does not use cellular LTE signals to produce an estimate of its state (i.e., the AGV only uses GNSS signals). These scenarios demonstrate that utilizing the freely available cellular signals in the environment for AGV navigation a) reduces the position estimation error and b) increases the number of feasible paths to the target point.
2) Scenario 3 compares the two path planning algorithms which a) assume fixed GNSS satellite geometry and b) consider GNSS satellite motion, for a long travel time (long trajectory). This scenario demonstrates the effect of satellite motion on the performance of each of the algorithms.
3) Scenario 4 considers different combinations of receivers: global positioning system (GPS) only, GPS + cellular, GPS + Galileo, and GPS + Galileo + cellular, to study the impact of adding different types of signals.

The experimental study was conducted on a ground vehicle driving in downtown Riverside, CA, USA, using real GPS and LTE signals. Three driving scenarios are considered, in which we have the following.

1) Scenario 1 compares the experimental navigation performance with the performance simulated by the path planning generator. A close match is demonstrated between the optimal path generated experimentally and in simulation.
2) Scenario 2 evaluates the navigation performance when the vehicle traverses the shortest path, which is an infeasible path according to the path planning generator. This scenario demonstrates that the path planning generator was able to predict poor (unsafe) navigation performance.
3) Scenario 3 considers long travel time (long trajectory) and compares the two path planning approaches which a) assume fixed GNSS satellite geometry and b) consider GNSS satellite motion. This scenario demonstrates an improved navigation performance in the path planning generator that accounts for GNSS satellite motion.

The significance of the proposed AGV path planning framework is threefold and is clearly demonstrated in the simulation and experimental results herein. First, it is shown that using cellular signals in the environment "opens up" new areas to navigate reliably and safely, which were infeasible with GNSS only. This alleviates the need to equip the vehicle with additional high-grade sensors that may violate cost, size, weight, and power (C-SWaP) constraints. Second, it is shown that the proposed approach can successfully predict whether the AGV's paths satisfy or violate a desired position estimation uncertainty. This is crucial for safety considerations as the shortest (or some other path) may not be safe to traverse. Third, the optimal path accounts for both distance and position mean-squared error (MSE) to ensure that lengthy, yet safe, paths (e.g., paths that require the AGV to leave and re-enter the urban environment) are deweighted.

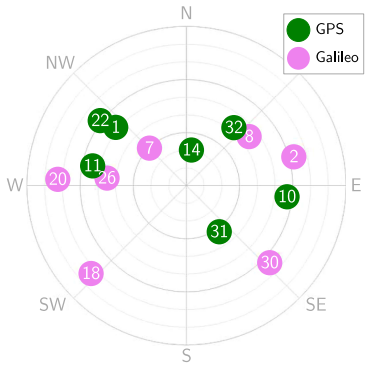

Fig. 1. Skyplot showing elevation and azimuth angles of GNSS satellites over Riverside, CA, USA, at 11:00 A.M. UTC, August 23, 2018. The numbers correspond to the pseudorandom noise code for each GPS and Galileo satellite [19], [20]. Data source: [21].

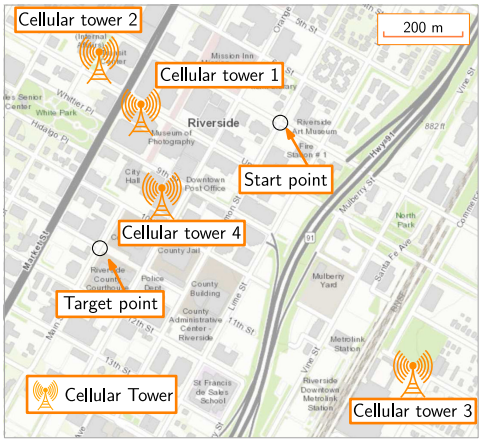

Fig. 2. Simulation environment showing start and target points and location of cellular base stations. This figure was obtained with ArcGIS [14].

III. SIMULATION STUDY

This section presents simulation results evaluating the performance of the path planning approach developed in [5].

A. Simulation Environment Setup

The simulation environment considered an AGV navigating downtown in Riverside, CA, USA. A 3-D building map of this environment was obtained from ArcGIS [16]. The GNSS satellite constellations comprised GPS and Galileo satellites. Fig. 1 illustrates the GNSS satellites' skyplot over Riverside at time $t = 11{:}00$ A.M., coordinated universal time (UTC), on August 23, 2018. The elevation and azimuth angles for both GPS and Galileo satellites were obtained using the PyEphem Python library [17]. Satellites with an elevation angle less than 15° were not used, as signals from these satellites tend to be severely degraded due to ionosphere, troposphere, and multipath [18].

Fig. 2 illustrates the simulation environment. The simulation settings for all four scenarios are summarized in Table I.

TABLE I
Simulation Settings

Parameter	Definition	Value
N	Number of GNSS satellites	14
M	Number of cellular base stations	4
t	Time in UTC (Scenario 1 & 2)	August 23, 2018, 11:00 am
$\{\sigma^2_{\text{gnss,n}}\}_{n=1}^{N}$	GNSS measurement noise variance	5 m^2
$\{\sigma^2_{\text{cell,m}}\}_{m=1}^{M}$	Cellular measurement noise variance	5 m^2
X	Number of impulses	An output of Wireless Insite
$a_i(x)$	Complex amplitude of signal path x and LTE symbol i	An output of Wireless Insite
$\tau_i(x)$	Path delay between the x-th impulse to the LOS path	An output of Wireless Insite
T_s	Sampling interval	3.25×10^{-8} s
L	Number of subcarrier symbols in the pilot sequence	200
ξ	Correlator spacing in the LTE receiver tracking loop	0.5
$\tilde{e}_\theta$	Symbol timing error	0

B. GNSS Simulation

GNSS signal reliability maps were generated. The GNSS satellite ephemeris data was found on the North American Aerospace Defense Command two-line element data set [22]. A 3-D building map was obtained from ArcGIS. The accuracy of the map is expected to be around 4.13 m based on a study of OpenStreetMap [16], [23]. A Python toolbox in ArcGIS was created to generate point features with reliability map information for a specified time interval. GNSS LOS was calculated by generating a line feature of fixed length along the LOS between the GNSS satellite and the point feature location. GNSS LOS was calculated at 5-s intervals, and times with changed visibility were recorded as tuples.

C. Multipath Simulation

Pseudorange biases caused by multipath were simulated. The complex channel impulse responses on a grid of receiver locations were generated using Wireless Insite X3D model [24] to calculate multipath bias $b_{m,p}$ according to

$$b_{m,p} \triangleq \chi_m + c\tau_i(0) - d_{\text{LOS}}, \quad m = 1, \ldots, M \qquad (1)$$

for each receiver location index p. In (1), we have the following.

1) c is the speed of light.
2) d_{LOS} is the length of the LOS path and is equal to the distance between the receiver and the transmitter in each simulated receiver location.
3) $\tau_i(0)$ is the time of flight of the first received peak and is an output of Wireless Insite.
4) χ_m is the multipath interference bias, calculated from (7) and (8) in [5]. The parameters to construct χ_m are given in Table I, among which X, $a_i(x)$, and $\tau_i(x)$ are outputs of Wireless Insite.

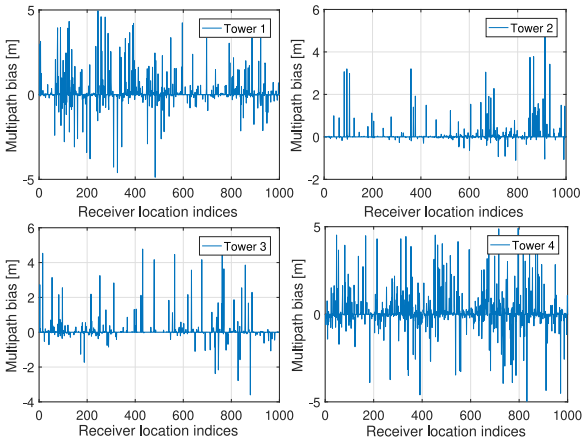

Fig. 3. Simulated induced multipath bias for all cellular base stations obtained from (1).

TABLE II
Scenario 1 Thresholds

Parameter	Definition	Value
$\bar{r}_{max}$	Position bias threshold	4 m
$\bar{\lambda}_{max}$	Eigenvalue constraint threshold	4 m^2
$\eta_{\max}$	Pseudorange error threshold	1 m
η_m	Weighted pseudorange error threshold	$\sqrt{5}$ m

The simulated induced multipath biases $\{b_{m,p}\}_{m=1}^{4}$ obtained from (1) for all four transmitters and $\{p_i\}_{i=1}^{1000}$ receiver locations with a spacing of 8 m are shown in Fig. 3. It is worth noting that the path planning generator evaluates the position MSE calculated using the LTE measurement variance and multipath-induced biases but does not generate simulated LTE pseudorange measurements.

D. Simulation Scenario Description

The output of the path planning generator is studied over four scenarios. In the first two scenarios, two AGVs were considered with the same start and target positions and time of departure. The optimization problem for each AGV used the same threshold values $\bar{\lambda}_{\max}$ and $\bar{r}_{\max}$. The optimal and feasible paths for both vehicles were calculated using Approach A described in [5], which does not account for GNSS satellite motion. AGV A was equipped with only GPS and Galileo receivers, while AGV B was equipped with GPS, Galileo, and cellular LTE receivers. The receiver clocks were synchronized for each vehicle, and the appropriate matrix $\mathbf{B}$ was used (see [5, (5)]).

In the third scenario, an AGV was equipped with GPS, Galileo, and cellular LTE receivers. The AGV prescribed a long trajectory, with different start and target locations from the first two scenarios. A trajectory is considered long if it is expected to take longer than 15 min to traverse or if there is a sharp change in the GNSS LOS along the path. The optimal and feasible paths were calculated using the following: 1) Approach A: does not account for GNSS satellite motion; 2) Approach B: accounts for GNSS satellite motion [5].

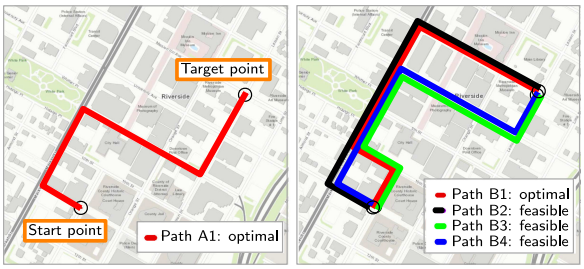

Fig. 4. Simulation results for Scenario 1. (a) Optimal path for AGV A, generated after relaxing the eigenvalue constraint from $\bar{\lambda}_{\max} = 4$ to $\bar{\lambda}_{\max} = 4.44$. (b) Optimal path and three feasible paths for AGV B without relaxing the eigenvalue constraint (i.e., with $\bar{\lambda}_{\max} = 4$). The optimal path Path B1 was shorter and produced less total RMSE than all other paths: Paths A1, B2, B3, and B4. This figure was obtained with ArcGIS [14].

TABLE III
Scenario 1 Results

	Path	Distance	Total RMSE	Maximum eigenvalue	Cost function value
AGV A	Path A1*	1006 m	4.37 m	4.44 m^2	16397
AGV B	Path B1	995 m	3.91 m	3.53 m^2	13108
	Path B2	1016 m	3.91 m	3.74 m^2	13158
	Path B3	1006 m	3.95 m	3.91 m^2	13358
	Path B4	1004 m	3.96 m	3.74 m^2	13408

*No feasible path was found for AGV A. This path was found after relaxing the eigenvalue constraint.

In the fourth scenario, four receiver combinations were considered: 1) GPS only, 2) GPS + cellular, 3) GPS + Galileo, and 4) GPS + Galileo + cellular. The position root mean squared error (RMSE) and maximum eigenvalue metrics were calculated over a few locations to analyze the impact of adding receivers to the simulated positioning accuracy.

E. Simulation Results

1) *Scenario 1:* Table II shows the thresholds used for both AGV A and AGV B. The user-specified thresholds are $\bar{r}_{\max}$ and $\bar{\lambda}_{\max}$, from which $\eta_{\max}$ is computed according to (16) in [5], and η_m corresponds to the mth element of $\mathbf{R}_a^{-\mathsf{T}}\mathbf{1}_{(\bar{N}+\bar{M})\times 1}\eta_{\max}$. The thresholds were chosen such that $\bar{r}_{\max} + \sqrt{\bar{\lambda}_{\max}}$ is approximately half the width of the street. The thresholds were chosen to bound the error statistics such that the vehicle does not calculate position to be in the middle of a building or at a different location index further up the street. It is important to know the correct closest location index because the set of reliable transmitters is different for each location index. Using the reliable transmitters at an adjacent location index can cause the AGV-mounted receiver to use measurements that are not reliable.

For the given simulation settings, AGV A had *no* feasible path which satisfies the constraints. One path was returned by the path planning generator by *relaxing* the eigenvalue constraint to $\bar{\lambda}_{\max} = 4.44\ m^2$. Fig. 4(a) illustrates this path. Table III presents this path's distance, total RMSE,

TABLE IV
Scenario 2 Thresholds

Parameter	Definition	Value
$\bar{r}_{max}$	Position bias threshold	4 m
$\bar{\lambda}_{max}$	Eigenvalue constraint threshold	5 m^2
$\eta_{\max}$	Pseudorange error threshold	$\frac{2}{\sqrt{5}}m$
η_m	Weighted pseudorange error threshold	2 m

maximum eigenvalue, and the cost function value (see [5, (12)] for optimization problem). For a given path π, the total RMSE was calculated according to

$$\text{Total RMSE} = \sqrt{\frac{\sum_{p\in\pi} \text{MSE}(p)}{h(\pi)}}$$

where $h(\cdot)$ denotes the number of locations in path π. In contrast, AGV B had four feasible paths *without* the need to relax the eigenvalue constraint (i.e., with $\bar{\lambda}_{\max} = 4$), with Path B1 being the optimal path. Fig. 4(b) illustrates these paths and Table III compares them.

The following can be concluded. First, including cellular LTE signals made the optimization problem feasible, without having to relax the constraint. Second, including cellular LTE signals resulted in several feasible paths to choose from (besides the optimal path), which could be useful if other considerations arise. Third, while the optimal path ended up yielding the shortest distance together with the total RMSE, a tradeoff between the shortest path and the total RMSE can be seen in the other feasible paths (e.g., Path B2 has lower total RMSE than Path B3 but has longer distance).

2) *Scenario 2:* This scenario is similar to Scenario 1, except that the eigenvalue constraint is relaxed even further to obtain several feasible paths for AGV A. Table IV shows the new thresholds used for both AGV A and AGV B.

By changing the constraints from Scenario 1, the number of feasible paths for AGV A increased from zero to two, while for AGV B, they increased from 4 to 12. Fig. 5 illustrates these paths and Table V compares them.

The following can be concluded. First, while both AGV A and AGV B found optimal and feasible paths, the optimal path for AGV B was significantly shorter than that for AGV A. Hence, utilizing cellular signals "opened up" areas in the environment that were otherwise infeasible with GNSS only. Second, slightly relaxing the constraint resulted in many new feasible paths versus Scenario 1, with the optimal path, Path B1, in Scenario 2 being reasonably shorter than the optimal path in Scenario 1 (namely, 33% shorter) with a slightly larger RMSE (namely, 11% higher). It should be noted that in a realistic scenario, if the designer found that there would be no feasible paths for the vehicle, a receiver for another GNSS constellation (or additional sensors) can be added, instead of adjusting the constraints.

3) *Scenario 3:* Tables II and VI show the simulation settings for this scenario. The simulation settings were

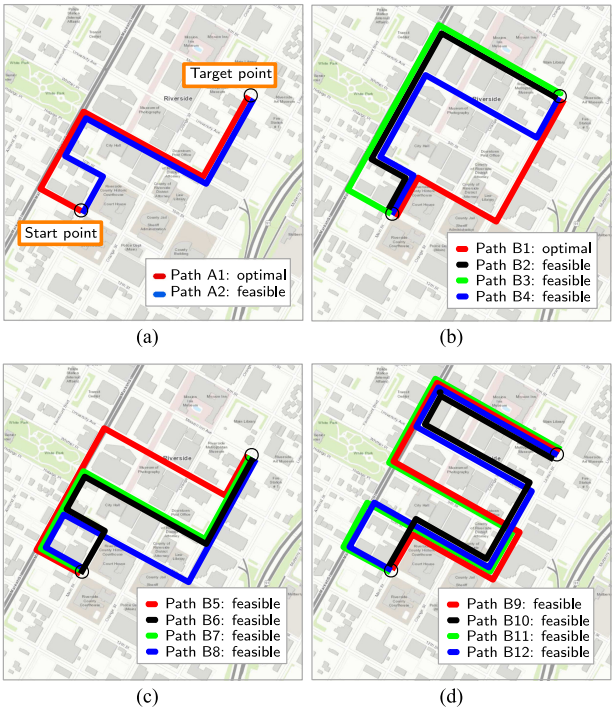

Fig. 5. Simulation results for Scenario 2. (a) Feasible paths for AGV A, where Path A1 is the optimal path. (b) Four feasible paths for AGV B which produced the lowest cost function, i.e., Paths B1–B4. (c) Paths B5–B8 for AGV B in order of lowest to highest cost function value. (d) Paths B9–B12 for AGV B in order of lowest to highest cost function value. This figure was obtained with ArcGIS [14].

TABLE V
Scenario 2 Results

	Path	Distance	Total RMSE	Maximum eigenvalue	Cost function value
AGV A	Path A1	1006 m	4.37 m	4.44 m^2	16397
	Path A2	1013 m	4.44 m	4.44 m^2	17012
AGV B	Path B1	748 m	4.34 m	4.28 m^2	11724
	Path B2	995 m	3.91 m	3.53 m^2	13108
	Path B3	1016 m	3.91 m	3.74 m^2	13158
	Path B4	1006 m	3.95 m	3.74 m^2	13358
	Path B5	1004 m	3.95 m	3.74 m^2	13408
	Path B6	1013 m	3.97 m	4.28 m^2	13412
	Path B7	1006 m	3.97 m	4.28 m^2	13462
	Path B8	1014 m	4.17 m	4.28 m^2	14605
	Path B9	1493 m	4.08 m	4.20 m^2	21519
	Path B10	1491 m	4.18 m	4.28 m^2	22515
	Path B11	1750 m	4.11 m	4.28 m^2	24401
	Path B12	1756 m	4.11 m	4.28 m^2	25397

TABLE VI
Scenario 3 Settings

Parameter	Definition	Value
t	Time in UTC	December 26, 2018, 3:04 pm
v_{AGV}	Vehicle speed	3.2 m/s
ζ	Search space size for path planning generator	4534

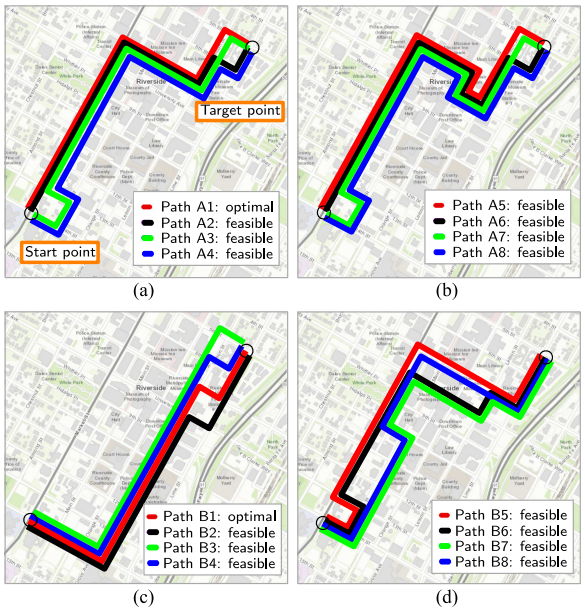

Fig. 6. Simulation results for Scenario 3. (a) Four feasible paths from Approach A which produced the lowest cost function, i.e., Paths A1–A4. (b) Paths A5–A8 from Approach A in order of lowest to highest cost function value. (c) Paths B1–B4 from Approach B in order of lowest to highest cost function value. (d) Paths B5–B8 from Approach B in order of lowest to highest cost function value. This figure was obtained with ArcGIS [14].

chosen at a time when there were sharp changes in the costs and constraints over the duration of the AGV's trajectory due to GNSS satellite motion. The value ζ was chosen such that the search space for Approach B included all paths that were feasible using Approach A.

For the given simulation settings, there are eight feasible paths according to Approach A, and 279 feasible paths according to Approach B. Fig. 6 shows the first eight feasible paths using either approach and Table VII compares them.

The following can be concluded. First, new feasible paths became available in Approach B. There were 48 feasible paths with lower cost than Path A1. This occurred because after the start time, there was a significant decrease in the maximum eigenvalue in several areas in the road network, which resulted in a large increase in the number of feasible paths. Clearly, there was large discrepancy between the simulation results of both approaches, which demonstrates that accounting for satellite motion is necessary for long trajectories. Second, there were feasible paths according to Approach A that were in fact infeasible, e.g., Paths A1 (the optimal path), A2, A5, and A6. An AGV that takes any of these paths will suffer from a navigation performance violating the desired constraints. Even if the optimal path for Approach A was the same as that of Approach B, the table of reliable GNSS satellites and cellular base stations produced by Approach A does not account for satellite motion and may become unusable as GNSS satellites' LOS geometry changes over long durations. This may cause the AGV to ignore measurements that are in fact reliable or accept measurements that are unreliable. This result demonstrates the importance of accounting for satellite motion for long trajectories.

TABLE VII
Scenario 3 Results

	Path	Distance	Total RMSE	Maximum eigenvalue	Cost function value
Approach A	Path A1	1600 m	2.97 m	3.22 m^2	14934
	Path A2	1603 m	2.97 m	3.22 m^2	15029
	Path A3	1862 m	2.94 m	2.90 m^2	17042
	Path A4	1865 m	2.94 m	2.90 m^2	17137
	Path A5	1854 m	2.97 m	3.22 m^2	17190
	Path A6	1857 m	2.97 m	3.22 m^2	17285
	Path A7	2116 m	2.94 m	2.90 m^2	19298
	Path A8	2119 m	2.94 m	2.90 m^2	19393
Approach B	Path B1	1605 m	2.84 m	3.55 m^2	12336
	Path B2	1608 m	2.84 m	3.55 m^2	12526
	Path B3	1609 m	2.82 m	3.55 m^2	13165
	Path B4	1612 m	2.83 m	3.55 m^2	13345
	Path B5	1864 m	2.76 m	3.69 m^2	13829
	Path B6	1855 m	2.80 m	3.69 m^2	13831
	Path B7	1854 m	2.83 m	3.69 m^2	13861
	Path B8	1863 m	2.79 m	3.69 m^2	13866

4) *Scenario 4:* This scenario compares four receiver combinations: 1) GPS only, 2) GPS + cellular, 3) GPS + Galileo, and 4) GPS + Galileo + cellular. The position RMSE and maximum eigenvalue metrics are calculated over a few locations to demonstrate the impact of adding receivers to the expected positioning accuracy. The path planning metrics are calculated using the simulation settings in Table IV. Fig. 7 shows the position RMSE and maximum eigenvalue metrics.

Based on Fig. 7, it is obvious that using receivers 1) and 4) is expected to yield the worst and best navigation performance, respectively. This can be seen based on both the position RMSE and eigenvalue constraint metrics. The RMSE with receiver 3) was lower than 1) in some locations. This result is expected because more Galileo satellites than cellular base stations were present (namely, 7 versus 4). However, there are some locations where receiver 2) outperforms 3). This is especially true for the maximum eigenvalue metric, which corresponds to the maximum position uncertainty and the upper bound on the position bias. It can be seen that there is one location where the maximum eigenvalue constraint is satisfied for 2) but not for 3). This shows that although 3) performs better than 2) for many locations, there are some locations that using cellular signals can "open up" areas in the environment that were otherwise infeasible with GNSS only.

IV. EXPERIMENTAL STUDY

This section presents experimental results for ground vehicle path planning in an urban environment with real GPS and cellular LTE signals.

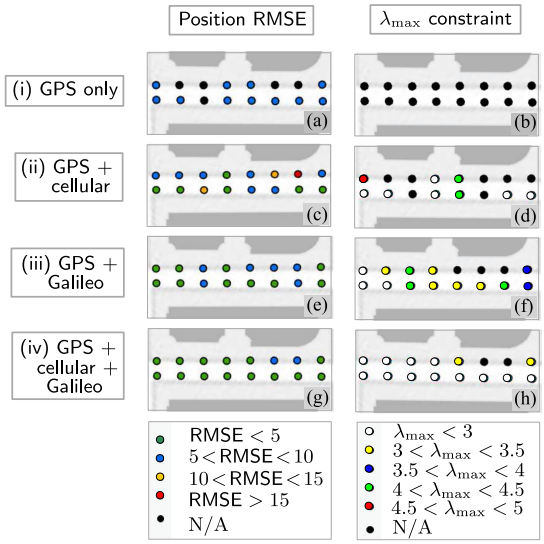

Fig. 7. Simulation results for Scenario 4. The shown receiver combinations are (a)–(b) GPS only, (c)–(d) GPS + cellular, (e)–(f) GPS + Galileo, and (g)–(h) GPS + Galileo + cellular. The left column (a), (c), (e), (g) corresponds to simulated position RMSE. The right column (b), (d), (f), (h) corresponds to the simulated largest eigenvalue metric. N/A corresponds to the situation in which the vehicle-mounted receiver did not have a sufficient number of measurements to estimate the vehicle's position. This figure was obtained with ArcGIS [14].

TABLE VIII
Characteristics of the LTE Base Stations

Tower	Service provider	Carrier frequency (MHz)	Cell ID	Bandwidth (MHz)
1	AT&T	1955	348-350	20
2	AT&T	1955	219	20
3	Verizon	2145	392	20
4	Verizon	2145	79	20

A. Experimental Setup and Scenario Description

A vehicle is equipped with two consumer-grade omnidirectional Laird antennas [25] to receive cellular LTE signals at two frequencies specified in Table VIII. The vehicle's position is taken as the midpoint of the antennas. The cellular LTE signals were down-mixed and sampled using a National Instruments (NI) dual-channel universal software radio peripheral (USRP)–2954R, driven by a GPS-disciplined oscillator [26]. The vehicle was also equipped with a Septentrio AsteRx-i V integrated GNSS and inertial measurement unit (IMU) module, which is equipped with a dual antenna, multifrequency GNSS receiver, and a Vectornav VN-100 micro-electromechanical system IMU. Septentrio's postprocessing software development kit (PP-SDK) was used to process carrier phase observables collected by the AsteRx-i V and by a nearby differential GPS base station to obtain a carrier phase-based navigation solution. This integrated GNSS-IMU real-time kinematic (RTK) system was used to produce the vehicle's ground truth path. The GNSS receiver also produced GPS pseudorange measurements. Cellular LTE pseudorange measurements were produced with the Multi-channel Adaptive TRansceiver Information eXtractor (MATRIX) software-defined receiver [13], [27]. The experimental setup is shown in Fig. 8.

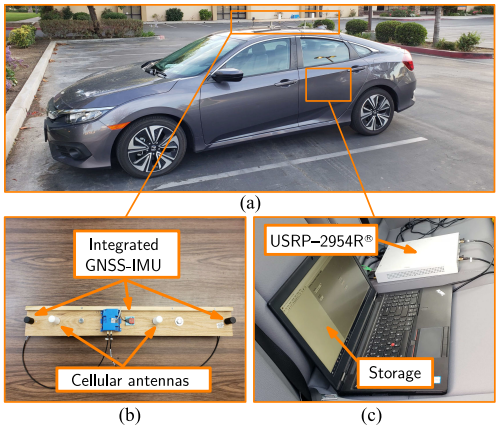

Fig. 8. Experimental setup. (a) Vehicle used to conduct the experiment, equipped with AsteRx-i V GNSS-IMU module, antennas, USRP–2954R, and laptop for storage and processing. (b) Hardware setup mounted on top of the vehicle. (c) Hardware setup placed inside the vehicle.

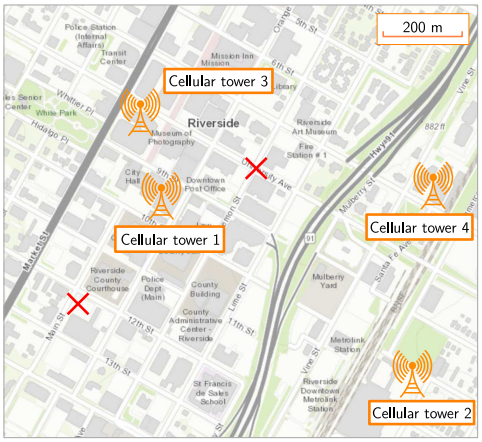

Fig. 9. Location of four cellular LTE base stations in downtown Riverside, CA, USA whose signals were used. Red X's signify locations where the measurement noise variances and cellular clock bias parameters were calculated. This figure was obtained with ArcGIS [14].

The experiment was conducted in downtown Riverside, CA, USA. The characteristics of the four LTE base stations are summarized in Table VIII and their locations are depicted in Fig. 9. The GPS receiver and LTE receiver clocks were not synchronized, and the appropriate matrix **B** was used (see [5, (6)]). The red "X" signifies locations where the vehicle was stationary for a few seconds, during which the measurement noise variances and cellular clock bias parameters were calculated.

Three scenarios were considered. The first scenario compares the experimental navigation performance (i.e., path length, total RMSE, maximum eigenvalue, cost function, etc.) versus the navigation performance predicted by the offline path planning generator. Eight GPS satellites were present at the time of the experiment and four LTE base stations were used. Fig. 10 depicts the start and target points for the ground vehicle. The path planning approach

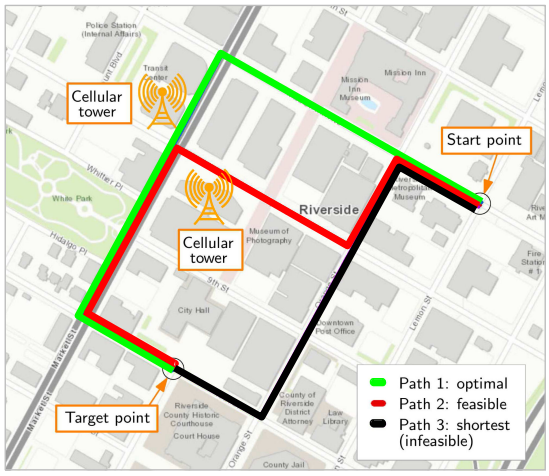

Fig. 10. Path planning generator results: Path 1: optimal; Path 2: feasible; and Path 3: shortest between the start and target points but is infeasible as it violates the constraints. This figure was obtained with ArcGIS [14].

TABLE IX
Experiment Settings for Scenarios 1 and 2

Parameter	Definition	Value
N	Number of satellites	8
M	Number of cellular base stations	4
t	Start time (UTC)	August 24, 2018, 6:34 am
$\bar{r}_{max}$	Position bias threshold	15 m
$\bar{\lambda}_{max}$	Eigenvalue constraint threshold	30 m^2
$\eta_{\max}$	Pseudorange error threshold	$\frac{2}{\sqrt{10}}$
K	Number of cellular measurements used for initialization	10
$\{\sigma^2_{\text{gnss,n}}\}_{n=1}^{N}$	GNSS measurement noise variance	$\{7.1, 5.1, 3.9, 6.9, 7.1, 6.7, 5.8, 9.5\}$ m^2
$\{\sigma^2_{\text{cell,m}}\}_{m=1}^{M}$	Cellular measurement noise variance	$\{8.7, 4.4, 7.8, 4.6\}$ m^2

described in Section III was executed offline with the settings in Table IX. It is worth noting that cellular towers 1 and 3 were surrounded by tall buildings. There are also tall buildings between towers 1 and 3 and the location where the measurement noise variances were calculated (red X's in Fig. 9). It is suspected that this caused the cellular measurement noise variances from towers 1 and 3 to higher than those from towers 2 and 4.

Because the Galileo constellation was not used in the experimental study, the dilution of precision (DOP) and multipath-induced bias will be higher compared to the simulation study, leading to higher predicted constraint metrics. Therefore, to allow for feasible paths, the constraints are relaxed in the experimental study. Though this does not follow the rule for constraint selection discussed in Section III-E1, the offline path planning generator output and experimental results can still be compared as the settings used in each are identical. It should be noted that in a realistic scenario, if the designer found that there would be no feasible paths for the vehicle, a receiver for another GNSS constellation (or additional sensors) can be added, instead of adjusting the constraints. An experiment with multiple GNSS constellations can be explored in future work. The spacing between location indices where the position MSE was generated was 8 m. The LTE measurement noise variances were calculated using the sample variance from received pseudoranges, while the vehicle was stationary over $K = 100$ samples. The perturbation parameters $\hat{\epsilon}_m$ and $\widehat{\sigma^2_{\epsilon,m}}$ were also calculated, while the vehicle was stationary over $K = 10$ samples. The thresholds $\bar{r}_{\max}$ and $\bar{\lambda}_{\max}$ are relaxed compared to the simulation study because the Galileo constellation is not used. The path planning generator returned an optimal path and a feasible path depicted in Fig. 10.

TABLE X
Experiment Settings for Scenario 3

Parameter	Definition	Value
v_{AGV}	Vehicle speed	3.2 m/s
t	Start time (UTC)	December 26, 2018, 3:00 pm
$\{\sigma^2_{\text{gnss,n}}\}_{n=1}^{N}$	GNSS measurement noise variance	$\{7.7, 4.5, 5.6, 7.2, 4.9, 9.0, 8.6, 8.7\}$ m^2

The second scenario evaluates the navigation performance if the vehicle chooses to take the shortest path (Path 3 in Fig. 10) instead of the optimal or feasible path. The settings for Scenario 2 are identical to those in experimental Scenario 1.

The third scenario compares Approach A (does not account for satellite motion) and Approach B (accounts for satellite motion). A vehicle was driven along a long trajectory, which was infeasible according to Approach A but feasible according to Approach B. The experimental results along this path were compared to the offline path planning generator output results from Approaches A and B. Table X provides the settings for Scenario 3 that differ from Scenario 1.

B. Experimental Results

1) *Scenario 1:* The purpose of this scenario is to compare the offline path planning generator output results with the experimental navigation results. The vehicle was driven along the optimal path, then the feasible path, and it was assumed that the satellite geometry over the two paths did not change drastically. The time difference between the two paths was 5 min and 40 s, which is below the threshold time for long trajectories (15 min). It was also confirmed that there are no sharp changes in the GNSS reliability maps along the path. Table XI compares the navigation performance (i.e., path length, total RMSE, maximum eigenvalue, cost function, etc.) along the optimal and feasible paths returned by the simulated results versus those returned experimentally.

Note the close match between the offline path planning generator output and experimental navigation performance. In particular, despite the differences in the offline path planning generator output and experimental cost function

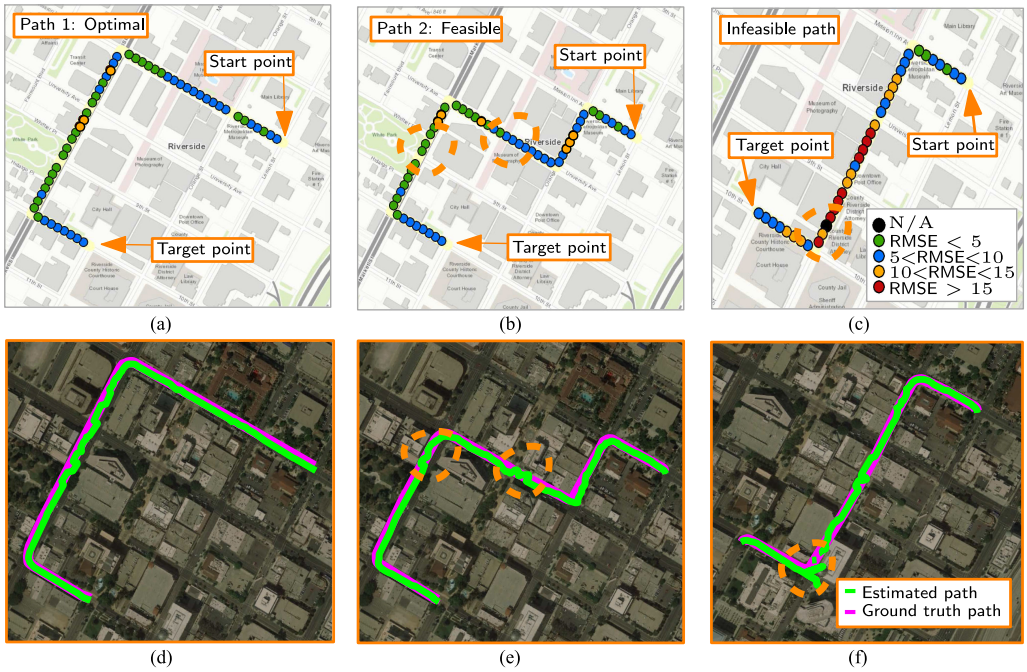

Fig. 11. Offline path planning generator output results (referred to as simulated) and experimental results along (a), (d) optimal path; (b), (e) feasible path; and (c), (f) infeasible path. (a), (b), and (c) show the simulated RMSE values at locations along the path, while (d), (e), and (f) compare the vehicle's experimentally estimated path from GNSS and cellular signals versus the ground truth path from the GNSS-IMU with RTK module. The dashed circle in (c) specifies the area in which the simulator did not have a sufficient number of measurements to estimate the vehicle's position (corresponding to an RMSE of N/A), which matches the same area in (f) at which there were not sufficient pseudorange measurements from GNSS and cellular signals to estimate the vehicle's position. This figure was obtained with ArcGIS [14].

TABLE XI
Scenario 1: Offline Path Planning Generator Output Results (Referred to as Simulation) and Experimental Navigation Results Along Optimal and Feasible Paths

	Path length		Total RMSE	
Path	**Simulation**	**Experiment**	**Simulation**	**Experiment**
Path 1: optimal	872 m	878 m	6.55 m	6.63 m
Path 2: feasible	884 m	886 m	7.19 m	7.47 m

	Maximum eigenvalue		Cost function value	
Path	**Simulation**	**Experiment**	**Simulation**	**Experiment**
Path 1: optimal	27.91 m^2	27.27 m^2	55939	42216
Path 2: feasible	27.91 m^2	26.85 m^2	68688	60029

values, Path 1 performed better than Path 2, as predicted by the path planning generator.

The offline path planning generator output RMSEs at each location are shown in Fig. 11. Also shown in Fig. 11 are the vehicle's ground truth path versus the experimentally estimated path with GPS and cellular LTE signals. It can be seen that the offline path planning generator output RMSE closely follows the experimentally estimated path.

Fig. 12 shows the offline path planning generator output versus experimental position errors for (a) optimal and (b) feasible paths. There are a few discrepancies between the generated and experimental results, which could be attributed to inaccuracies in the map. In one particular area of Fig. 11(b) (depicted with a dashed circle), the experimental RMSE was 19.51 m, while the generated RMSE at that area was about 5 m. This result can be seen in Fig. 12(b) (depicted with dashed circles) from 108 to 110 s. Note that the offline path planning generator output RMSE increases to 17.01 m shortly thereafter. There are also unexpectedly high experimental position errors that do not match the generated RMSE from 41 to 45 s. This may be due to the fact that the offline path planning generator does not account for attenuation due to trees (there was dense foliage near both areas). This result reveals that accurate knowledge of the environment could be crucial for accurately generating the position MSE. The foliage was not included in the 3-D map because it was not surveyed or available online prior to the experiment. However, existing software packages (e.g., Wireless Insite) could simulate foliage effects. There are also areas in Fig. 12(b) where the offline path planning generator output RMSE is larger than the experimental RMSE, such as from 60 to 80 s. This is a period of time where the vehicle was stationary, and the actual measurement noise variances may be smaller than those calculated in the initialization step. This can be addressed in future work by parameterizing the measurement noise variances according to the carrier-to-noise ratio (C/N_0) instead of assuming it to be constant.

2) *Scenario 2:* This scenario evaluates the navigation performance for a vehicle using Dijkstra's path planning algorithm to execute the path with the shortest length [28]. In other words, the path planning algorithm does not account

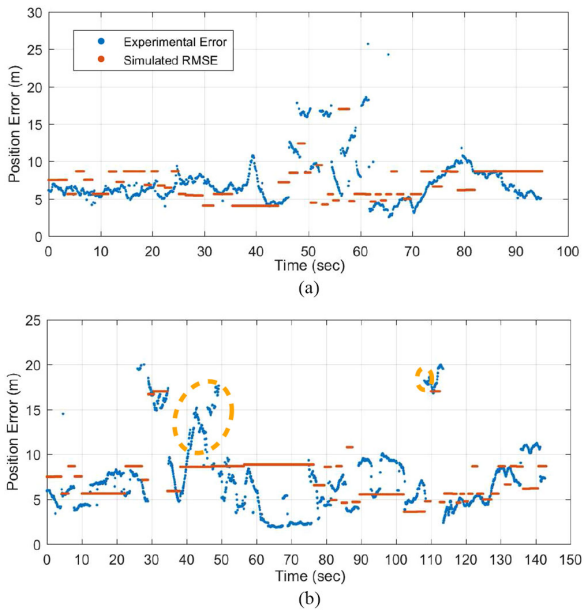

Fig. 12. Offline path planning generator output (referred to as simulated) position RMSE and experimental position error along (a) optimal path and (b) feasible path. Simulated position RMSE values are shown by red dots, while experimental position error is shown with blue dots.

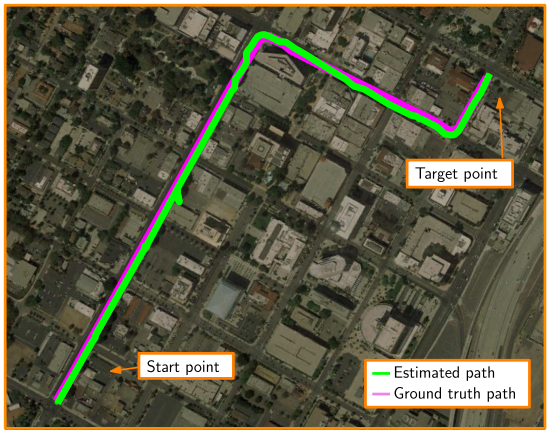

Fig. 13. Chosen path which is infeasible according to Approach A and feasible according to Approach B. Experimental results are shown of the vehicle's estimated path from GNSS and cellular measurements. This figure was obtained with ArcGIS [14].

TABLE XII
Scenario 3: Offline Path Planning Generator Output (Referred to as Simulation) and Experimental Navigation Results Along the Chosen Path

	Distance	Total RMSE	Maximum eigenvalue	Cost function value
Experiment data	1187 m	5.78 m	27.93 m^2	34890
Simulation data (Approach A)	1152 m	5.98 m	31.49 m^2	35773
Simulation data (Approach B)	1152 m	5.94 m	29.19 m^2	35369

for navigation performance: The cost function simply considers the distance, while both constraints are removed. Path 3 in Fig. 10 is chosen which has a corresponding distance of 629 m between the start and target points. As shown in Fig. 11(c) and (f), Path 3 was deemed infeasible by the path planning generator as several areas had a simulated RMSE over 20 m, and one area had an insufficient number of measurements to produce an estimate of the vehicle's state.

The experimental RMSE along the entire path was 12.12 m in areas where the navigation solution was computed, which is twice as large as the position RMSE of the other two paths. The dashed circle depicted in Fig. 11(f) shows the area where the vehicle was unable to estimate its position from GNSS and cellular signals, which is consistent with Fig. 11(c). This scenario highlights the importance of path planning to avoid situations where the AGV could fail to estimate its state.

3) *Scenario 3:* This scenario compares the offline path planning generator output navigation performances using Approach A and Approach B and compares the results with experimental data. The experimental data was collected along a path that was infeasible according to Approach A but feasible according to Approach B. This path is shown in Fig. 13

Table XII compares the navigation performance along this path as returned by the offline path planning generator output results versus those found experimentally.

It can be seen that the experimental results (total RMSE, maximum eigenvalue, and cost function) agree more with Approach B than Approach A. It should be noted that the vehicle's actual speed was nearly 6.7 m/s. These results demonstrate an improvement in the path planning generator when satellite motion is accounted for, even when the expected vehicle speed is not exact. The experimental results also show that the chosen path is feasible because it satisfies the constraint, which is consistent with Approach B but not consistent with Approach A. This shows that accounting for GNSS satellite motion can lead to prescribed paths that are shorter or have less error.

V. CONCLUSION

This article considered the problem where an AGV equipped with GNSS and cellular receivers desires to reach a target location by taking the shortest path with minimum position MSE, while guaranteeing that the bias in the position estimate and the position uncertainty are below desired thresholds. The prequel of this article discussed algorithms to generate signal reliability maps and path planning. This article presented simulation and experimental results demonstrating the efficacy and accuracy of the path planning approach for several driving scenarios. The simulation results revealed that the path planning approach 1) reduced the uncertainty about the AGV's position, 2) increased the number of feasible paths to choose from, which could be useful if other considerations arise (e.g., traffic jams and road blockages due to construction), and 3) yielded significantly shorter feasible paths, which would

otherwise be infeasible with GNSS signals alone. The experimental results carried out on a ground vehicle navigating in downtown Riverside, CA, USA, demonstrated a close match with the simulated results.

The prescribed optimal path is expected to be among the shortest paths in distance, while also accounting for position accuracy along the path. Additionally, this path avoids areas with large expected position errors, which could violate safety constraints. In some cases, the prescribed path may avoid urban canyons altogether and may direct the AGV to leave the urban environment and re-enter closer to the destination. In this case, it is recommended that the vehicle manufacturer adds additional radio navigation receivers or sensors to reduce the expected position error to meet safety constraints. Other error sources can be introduced in the path planning cost and constraints, such as GNSS multipath-induced bias, or inaccuracies in the building footprints that have been modeled in prior work [23]. Methods for GNSS and cellular visibility predictions can be improved through 1) comparing signal availability and received signal strength to 3-D map predictions using power and shadow matching [29]–[32], or 2) using a fish-eye camera to detect GNSS non-line-of-sight (NLOS) [33], [34]. The same costs and constraints can be evaluated with different navigation frameworks that use filtering techniques and sensor fusion. Integrity monitoring techniques [35]–[39] and map matching [40]–[43] can also be used to improve transmitter selection or augment the path planning cost function. Time-varying path planning in Approach B can be improved by using traffic information [44].

ACKNOWLEDGMENT

The authors would like to thank J. Khalife, K. Shamaei, and C. Simons for their help with data collection.

SONYA RAGOTHAMAN, *Member, IEEE*
University of California, Riverside, CA, USA

MAHDI MAAREF

ZAHER M. KASSAS, *Senior Member, IEEE*
University of California Irvine, CA, USA

REFERENCES

[1] T. Luettel, M. Himmelsbach, and H. Wuensche
Autonomous ground vehicles- concepts and a path to the future
In *Proc. IEEE*, vol. 100, no. *Special Centennial Issue*, May 2012, pp. 1831–1839,.

[2] Z. Kassas, P. Closas, and J. Gross
Navigation systems for autonomous and semi-autonomous vehicles: Current trends and future challenges
IEEE Aerosp. Electron. Syst. Mag., vol. 34, no. 5, pp. 82–84, May 2019.

[3] M. Maaref and Z. Kassas
Optimal GPS integrity-constrained path planning for ground vehicles
In *Proc. IEEE/ION Position, Location, Navigation Symp.*, Apr. 2020, pp. 655–660.

[4] S. Ragothaman
Path planning for autonomous ground vehicles using GNSS and cellular LTE signal reliability maps and GIS 3-D maps
Master's thesis, Univ. California, Riverside, Irvine, CA, USA, 2018.

[5] S. Ragothaman, M. Maaref, and Z. Kassas
Autonomous ground vehicle path planning in urban environments using GNSS and cellular signals reliability maps: Models and algorithms
IEEE Trans. Aerosp. Electron. Syst., to be published, doi: 10.1109/TAES.2021.3054690.

[6] K. Borre, D. Akos, N. Bertelsen, P. Rinder, and S. Jensen
Software-Defined GPS and Galileo Receiver: A Single-Frequency Approach. Cambridge, MA, USA: Birkhäuser, 2007.

[7] T. Pany
Navigation Signal Processing for GNSS Software Receivers. Norwood, MA, USA: Artech House, 2010.

[8] Z. Kassas, J. Bhatti, and T. Humphreys
A graphical approach to GPS software-defined receiver implementation
In *Proc. IEEE Global Conf. Signal Inf. Proc.*, Dec. 2013, pp. 1226–1229.

[9] M. Braasch and A. Dempster
Tutorial: GPS receiver architectures, front-end and baseband signal processing
IEEE Aerosp. Electron. Syst. Mag., vol. 34, no. 2, pp. 20–37, Feb. 2019.

[10] J. del Peral-Rosado *et al.*
Software-defined radio LTE positioning receiver towards future hybrid localization systems
In *Proc. Int. Commun. Satellite Syst. Conf.*, Oct. 2013, pp. 14–17.

[11] K. Shamaei, J. Khalife, and Z. Kassas
Exploiting LTE signals for navigation: Theory to implementation
IEEE Trans. Wireless Commun., vol. 17, no. 4, pp. 2173–2189, Apr. 2018.

[12] M. Driusso, C. Marshall, M. Sabathy, F. Knutti, H. Mathis, and F. Babich
Vehicular position tracking using LTE signals
IEEE Trans. Veh. Technol., vol. 66, no. 4, pp. 3376–3391, Apr. 2017.

[13] K. Shamaei and Z. Kassas
LTE receiver design and multipath analysis for navigation in urban environments
J. Inst. Navigation, vol. 65, no. 4, pp. 655–675, Dec. 2018.

[14] Esri
[Online]. Available: https://www.arcgis.com

[15] 3D buildings
[Online]. Available: https://3dbuildings.com/

[16] ArcGIS Downtown Buildings
[Online]. Available: https://services.arcgis.com/Fu2oOWg1Aw7azh41/arcgis/rest/services/DowntownBuildings/FeatureServer

[17] Pyephem
[Online]. Available: https://rhodesmill.org/pyephem

[18] E. Kaplan and C. Hegarty
Understanding GPS/GNSS: Principles and Applications, 3rd ed. Norwood, MA, USA: Artech House, 2017.

[19] GPS Navstar
Space segment/navigation user interfaces interface specification IS-GPS-200
Dec. 2015,
[Online]. Available: http://www.gps.gov/technical/icwg/

[20] GSC European Galileo open service signal in space interface control document
(Os Sis Icd) Dec. 2016,
[Online]. Available: https://www.gsc-europa.eu/electronic-library/ programme-reference-documents

[21] GNSS Radar
[Online]. Available: http://www.taroz.net/GNSS-Radar.html
[22] North American Aerospace Defense Command (NORAD) Two-line element sets
[Online]. Available: http://celestrak.com/NORAD/elements/
[23] H. Fan, A. Zipf, Q. Fu, and P. Neis
Quality assessment for building footprints data on OpenStreetMap
Int. J. Geographical Inf. Sci., vol. 28, no. 4, pp. 700–719, 2014.
[24] Remcom
[Online]. Available: https://www.remcom.com
[25] Laird Phantom 3 G/4 G multiband antenna NMO Mount White TRA6927M3NB
[Online]. Available: https://www.lairdtech.com/products/phantom-series-antennas
[26] National Instruments Universal Software Radio peripheral-2954R.
[27] Z. Kassas, J. Khalife, K. Shamaei, and J. Morales
I hear, therefore I know where I am: Compensating for GNSS limitations with cellular signals
IEEE Signal Process. Mag., vol. 34, no. 5, pp. 111–124, Sep. 2017.
[28] E. Dijkstra
A note on two problems in connexion with graphs
Numerische Mathematik, vol. 1, no. 1, pp. 269–271, Dec. 1959.
[29] S. Saab and Z. Kassas
Power matching approach for GPS coverage extension
IEEE Trans. Intell. Transp. Syst., vol. 7, no. 2, pp. 156–166, Jun. 2006.
[30] A. Irish, J. Isaacs, D. Iland, J. Hespanha, E. Belding, and U. Madhow
Demo: ShadowMaps, the urban phone tracking system
In *Proc. Annu. Int. Conf. Mobile Comput. Netw.*, Sep. 2014, pp. 283–286.
[31] J. Isaacs, A. Irish, F. Quitin, U. Madhow, and J. Hespanha
Bayesian localization and mapping using GNSS SNR measurements
In *Proc. IEEE/ION Position, Location, Navigation Symp.*, May 2014, pp. 445–451.
[32] L. Wang, P. Groves, and M. Ziebart
Smartphone shadow matching for better cross street GNSS positioning in urban environments
J. Navigation, vol. 69, no. 3, pp. 411–433, 2015.
[33] T. Suzuki and N. Kubo
N-LOS GNSS signal detection using fish-eye camera for vehicle navigation in urban environments
In *Proc. ION GNSS Conf.*, Sep. 2014, pp. 1897–1906.
[34] W. Wen, X. Bai, Y. Kan, and L. Hsu
Tightly coupled GNSS/INS integration via factor graph and aided by fish-eye camera
IEEE Trans. Veh. Technol., vol. 68, no. 11, pp. 10 651–10662, Nov. 2019.
[35] N. Velaga, M. Quddus, A. Bristow, and Y. Zheng
Map-aided integrity monitoring of a land vehicle navigation system
IEEE Trans. Intell. Transp. Syst., vol. 13, no. 2, pp. 848–858, Jun. 2012.
[36] A. El-Mowafy and N. Kubo
Integrity monitoring for positioning of intelligent transport systems using integrated RTK-GNSS, IMU and vehicle odometer
IET Intell. Transp. Syst., vol. 12, no. 8, pp. 901–908, Oct. 2018.
[37] N. Zhu, J. Marais, D. Betaille, and M. Berbineau
GNSS position integrity in urban environments: A review of literature
IEEE Trans. Intell. Transp. Syst., vol. 19, no. 9, pp. 2762–2778, Sep. 2018.
[38] M. Maaref and Z. Kassas
Measurement characterization and autonomous outlier detection and exclusion for ground vehicle navigation with cellular signals
IEEE Trans. Intell. Veh., vol. 5, no. 4, pp. 670–683, Dec. 2020.
[39] M. Maaref and Z. Kassas
Autonomous integrity monitoring for vehicular navigation with cellular signals of opportunity and an IMU
IEEE Trans. Intell. Transp. Syst., to be published, doi: 10.1109/TITS.2021.3055200.
[40] F. Li, P. Bonnifait, J. Ibanez-Guzman, and C. Zinoune
Lane-level map-matching with integrity on high-definition maps
In *Proc. IEEE Intell. Veh. Symp.*, Jun. 2017, pp. 1176–1181.
[41] C. Zinoune, P. Bonnifait, and J. Ibanez-Guzman
Sequential FDIA for autonomous integrity monitoring of navigation maps on board vehicles
IEEE Trans. Intell. Transp. Syst., vol. 17, no. 1, pp. 143–155, Jan. 2016.
[42] M. Maaref and Z. Kassas
Ground vehicle navigation in GNSS-challenged environments using signals of opportunity and a closed-loop map-matching approach
IEEE Trans. Intell. Transp. Syst., vol. 21, no. 7, pp. 2723–2723, Jul. 2020.
[43] Z. Kassas, M. Maaref, J. Morales, J. Khalife, and K. Shamaei
Robust vehicular localization and map matching in urban environments through IMU, GNSS, and cellular signals
IEEE Intell. Transp. Syst. Mag., vol. 12, no. 3, pp. 36–52, Jun. 2020.
[44] E. Nikolova
High-performance heuristics for optimization in stochastic traffic engineering problems
in *Proc. Large-Scale Sci. Comput.*, Jun. 2010, pp. 352–360.